ELSEVIER

Chemical Engineering Science 60 (2005) 1117–1126

Chemical Engineering Science

www.elsevier.com/locate/ces

CFD simulations of wall mass transfer for Taylor flow in circular capillaries

J.M. van Baten, R. Krishna*

Van 't Hoff Institute for Molecular Sciences, University of Amsterdam, Nieuwe Achtergracht 166, 1018 WV Amsterdam, The Netherlands

Abstract

Computational fluid dynamics is used to investigate the mass transfer from the liquid phase to the channel wall for Taylor flow of bubbles rising in circular capillaries. The separate influences of the Taylor bubble rise velocity, unit cell length, gas holdup, and liquid diffusivity on mass transfer were investigated for capillaries of 1.5, 2 and 3 mm diameter. A correlation is proposed for estimation of the wall mass transfer coefficient and this correlation has been tested against published experimental data.

Keywords: Taylor bubbles; Mass transfer; Capillary; CFD; Monolith reactors; Wall; Film

1. Introduction

Multiphase monolith reactors offer many potential advantages over trickle beds, slurry bubble columns and airlifts that include low-pressure drop, high mass transfer rates, and ease of scale up (Edvinsson and Cybulski, 1995; Kreutzer, 2003; Nijhuis et al., 2001; Stankiewicz, 2001). Monolith reactors are being applied in laboratory studies and in commercial practice for carrying out reactions such as hydrogenations. Provided the gas and liquid phases are uniformly distributed over the various channels of the monolith, commercial reactors of large dimensions can, in principle, be scaled up from information on the hydrodynamics, mass transfer, and mixing within a single channel that has dimensions typically in the 1–3 mm range (Boger et al., 2003; Roy et al., 2004). Inside each capillary, we usually have Taylor flow of gas bubbles, as shown schematically in Fig. 1a. In the development and design of monolith loop reactors for fast reactions, there are two mass transfer processes to reckon with: (a) transfer from the Taylor gas bubbles to the surrounding liquid phase, and (b) transfer from the liquid phase to the walls of the monolith channels. In recent work (van Baten and Krishna, 2004b) we had focussed on the mass transfer from Taylor bubbles to the surrounding liquid phase and used extensive computational fluid dynamics (CFD) simulations in order to develop a model, based on the penetration theory, to allow the prediction of the volumetric mass transfer coefficient $k_L a$ from information on the various hydrodynamic and system parameters. The focus of the current work is on mass transfer from the liquid phase to the walls of the *circular* capillary channels of monoliths.

Fig. 1b shows the liquid phase velocity profiles within a liquid "slug'' separating two Taylor bubbles (these profiles were obtained from CFD simulations to be described later). The recirculation of the liquid phase causes a significant enhancement to *radial* mass transfer within the slug. In Fig. 2a we illustrate this by replotting the experimental data of Bercic and Pintar (1997) in terms of the Sherwood number for wall mass transfer, $Sh \equiv k_w d_c/Đ$, as a function of the Graetz number $Gz_{\text{tube}} \equiv L_{\text{tube}}(1-\varepsilon_G)Đ/d_c^2 V_b$. Note that we include the liquid holdup in the definition of Gz_{tube}; the rationale will be clear in the discussions below. The experimental data for Taylor flow mass transfer are about one order of magnitude higher than the corresponding value for single-phase liquid flow ($\varepsilon_G = 0$) in circular tubes, for which $Sh = 1.62 Gz_{\text{tube}}^{-1/3}$, provided $Gz_{\text{tube}} < 0.05$ (Shah and London, 1978). The experimental data of Horvath et al. (1973) on wall Sherwood number also show a dependence on the ratio of the slug length to capillary diameter, L_{slug}/d_c (see Fig. 2b).

* Corresponding author. Tel.: +31 20 525 7007; fax: +31 20 525 5604.
E-mail address: R.Krishna@uva.nl (R. Krishna).

0009-2509/$ - see front matter © 2004 Elsevier Ltd. All rights reserved.
doi:10.1016/j.ces.2004.10.001

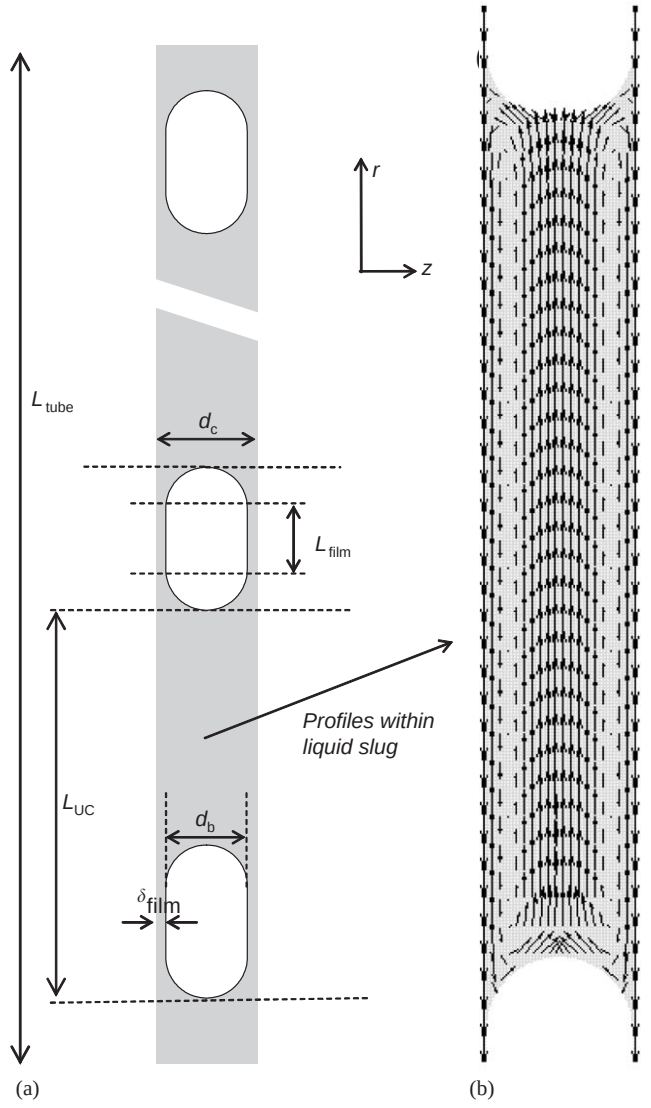

Fig. 1. (a) Schematic of Taylor bubble rise in a capillary and (b) liquid velocity vectors obtained from CFD simulations for $d_c = 3\,\text{mm}$, $V_b = 0.45\,\text{m/s}$, $L_{UC} = 0.025\,\text{m}$, $\delta_{\text{film}} = 48\,\mu\text{m}$, $\varepsilon_G = 0.272$, $L_{\text{film}} = 5.321\,\text{mm}$, $Đ = 1 \times 10^{-9}\,\text{m}^2/\text{s}$.

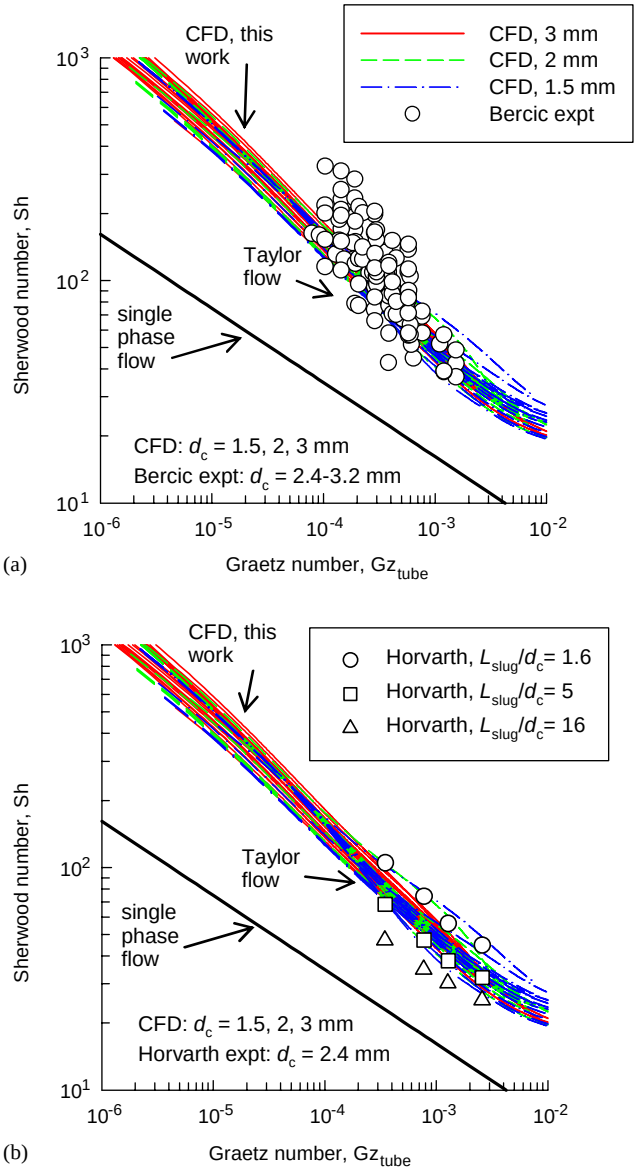

Fig. 2. Sherwood number for wall-mass transfer plotted against the Graetz number defined as $Gz_{\text{tube}} \equiv L_{\text{tube}}(1-\varepsilon_G)Đ/d_c^2 V_b$ for single phase flow and for Taylor flow in circular capillaries. (a) The symbols show the experimental data of Bercic and Pintar (1997) obtained in capillaries of diameters $d_c = 2.4$, 2.5 and 3.2 mm. The 2.5 mm capillary had a length $L_{\text{tube}} = 0.35\,\text{m}$, the 3.2 mm capillary had lengths of 0.25–0.27 m. (b) The symbols show the experimental data of Horvath et al. (1973) obtained in a capillary of $d_c = 2.4$ and three different slug lengths. Also plotted in (a) and (b) are all the CFD simulations carried out in this work for capillaries of diameters $d_c = 1.5$, 2 and 3 mm for a variety of hydrodynamic parameters as specified in Table 1.

Bercic and Pintar (1997) and Irandoust and Andersson (1988) have both put forward *empirical* correlations for estimation of the wall mass transfer coefficient k_w. Kreutzer (2003) and Kreutzer et al. (2001) have used axi-symmetric CFD simulations to determine the wall mass transfer coefficient, without explicitly accounting for the presence of the Taylor bubble and the resulting flow of liquid in the film surrounding the bubble. As we shall demonstrate in this paper, such estimations are rather optimistic for high gas holdups, long Taylor bubbles and long contact with the liquid film. The major objective of the present work is to use CFD in order to investigate wall mass transfer in the real situation including the presence of the Taylor bubble. Furthermore, we study the *separate* influences on *Sh* of various hydrodynamic and system parameters such as bubble rise velocity V_b, unit cell length L_{UC}, gas holdup ε_G, liquid phase diffusivity $Đ$, thickness of liquid film surrounding the Taylor bubble δ_{film}, and capillary diameter d_c. Such a study will provide insights into the mass-transfer mechanisms and allow more reliable scale up of monolith reactors. The second objective is to suggest a practical, engineering, correlation for estimation of *Sh*.

2. CFD model development

We consider an idealized geometry for the Taylor bubbles, consisting of two hemispherical caps and a cylindrical body. The Taylor bubble is considered as a "void", acting as a free surface with the surrounding liquid phase; see the computational domain shown in Fig. 3a. The influence of the assumption of hemispherical caps is of secondary importance to the mass transfer contributions from the wall. The distribution of velocities in the system is more important, and will not be influenced significantly by the precise shape of the interface, since the interface does not exert drag on the liquid. The volume-averaged mass and momentum conservation equations in the Eulerian framework are given by

$$\nabla \bullet \mathbf{u}_L = 0, \tag{1}$$

$$\rho_L \frac{\partial \mathbf{u}_L}{\partial t} + \nabla \bullet \left(\rho_L \mathbf{u}_L \mathbf{u}_L - \mu_L (\nabla \mathbf{u}_L + (\nabla \mathbf{u}_L)^{\mathrm{T}}) \right) = -\nabla p + \rho_L \mathbf{g}, \tag{2}$$

where ρ_L, $\mathbf{u}_L$ and μ_L represent, respectively, the macroscopic density, velocity and viscosity of the liquid phase, p is the pressure and $\mathbf{g}$ is the gravitational acceleration. Laminar flow conditions are assumed to prevail.

A commercial CFD package CFX, version 4.4, of ANSYS Inc., Canonsburg, USA was used to solve the equations of continuity and momentum. This package is a finite volume solver, using body-fitted grids. The grids are non-staggered and all variables are evaluated at the cell centres. An improved version of the Rhie–Chow algorithm (Rhie and Chow, 1983) is used to calculate the velocity at the cell faces. The pressure–velocity coupling is obtained using the SIMPLEC algorithm (van Doormal and Raithby, 1984). For the convective terms in Eqs. (1) and (2), the SUPERBEE-MUSCL differencing scheme was used (higher order upwind scheme with flux delimiters). A fully implicit backward differencing scheme was used for the time integration.

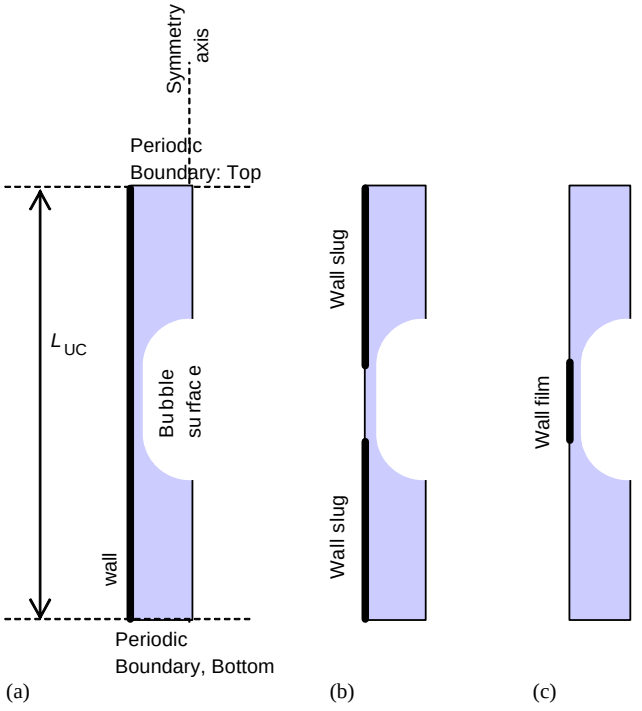

Fig. 3. (a) Schematic overview of the computational domain of unit cell with periodic boundary conditions at inlet and outlet, (b) highlights the wall–slug contribution to mass transfer and (c) highlights the wall–film contribution to mass transfer.

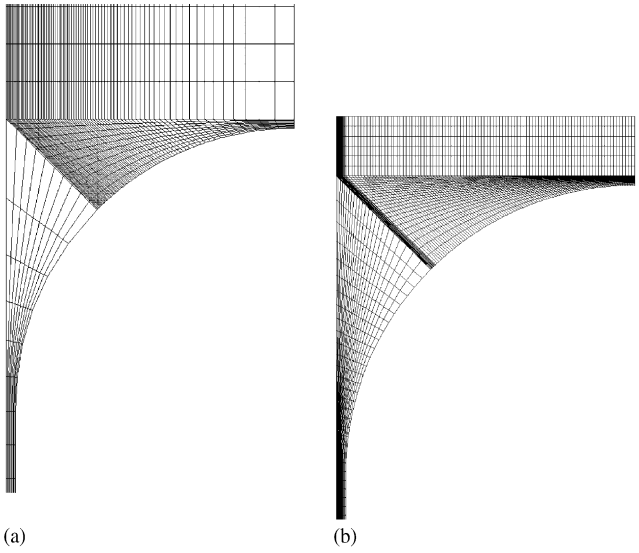

Fig. 4. (a) Schematic of coarse grid and (b) schematic of fine grid. The fine grid details are specified in Table 1.

The boundary condition was periodic in the vertical direction ($\mathbf{u}_{top} = \mathbf{u}_{bottom}$, $p_{top} = p_{bottom}$). The hydrostatic pressure drop of $\mathbf{g}\rho_L$ is added as a source term to the momentum balance Eq. (2) to correct for the periodic boundary conditions.

Simulations were performed in a reference frame in which the bubble is stationary and the system moves up with the bubble rise velocity V_b. At the outer wall, the boundary condition was set to $u_z = V_{wall} = -V_b$, $u_r = 0$, where r and z are the radial and axial coordinates. The bubble surface is specified as free-slip: $\mathrm{d}u_\perp/\mathrm{d}n = 0$ with $u_\perp$ being the velocity component in the direction of the bubble surface, and n is the normal direction to the bubble surface. At the axis of symmetry, we have: $\mathrm{d}u_z/\mathrm{d}r = 0$.

The simulations were carried out using axi-symmetric 2D grids using cylindrical coordinates. The calculation of the wall mass-transfer coefficient using CFD simulations was carried out in three consecutive campaigns.

In the *first campaign*, the mass and momentum transfer equations are solved for a *coarse grid* (typical coarse grid shown in Fig. 4a) to obtain the *steady-state* hydrodynamics. Using this velocity field solution as initial guess, the hydrodynamic steady state is re-calculated in a *second campaign* using a *fine grid* that has much smaller cells near the mass-transfer surfaces, i.e., the wall (see Fig. 4b). The steady-state

Table 1
Details of variations of parameters and grid cells used in the simulations

d_c (mm)	L_{UC} (mm)	V_b (m/s)	L_{film} (mm)	δ_{film} (μm)	ε_G (−)	Total number of grid cells	Smallest cell size (μm)
3	40	0.15, 0.3, 0.55	5.32	48	0.17	85,848	1.00
3	50	0.45	5.32	48	0.136	109,848	1.00
3	35	0.45	5.32	48	0.194	73,848	1.00
3	15, 20, 25, 30	0.45	5.32	48	0.227–0.453	61,848–25,848	1.00
3	40	0.45	6.60, 10.9, 15.1, 19.4	48	0.20–0.5	83,352–58,776	1.00
3	100	0.05, 0.1, 0.2, 0.3	51.4	48	0.5	141,336	1.00
2	40	0.15, 0.3, 0.45	5.97	32	0.170	66,620	0.60
2	15, 25, 40	0.45	5.97	32	0.170–0.453	66,620–21,620	0.60
2	100	0.05, 0.1, 0.2, 0.3, 0.4	52.1	32	0.5	115,612	0.60
1.5	40	0.15, 0.3, 0.45	6.29	24	0.170	90,312	0.40
1.5	15, 25, 40	0.45	6.29	24	0.17–0.453	90,312–28,812	0.40
1.5	100	0.05, 0.1, 0.2, 0.3, 0.4	52.4	24	0.5	149,400	0.40

solutions were typically obtained within 30,000–40,000 iterations and it was verified that convergence was indeed obtained.

From the converged hydrodynamics, the average liquid velocity is calculated from a summation over the cells at the top boundary of the computational domain:

$$u_{L,\text{domain}} = \frac{\sum_{\text{top}} \text{vol}_i u_i}{\sum_{\text{top}} \text{vol}_i}. \tag{3}$$

Here, vol_i is the volume of cell i and u_i is the vertical velocity in cell i. The summation in Eq. (3) is over the total number of cells at the top boundary. The *superficial* liquid velocity is now calculated from

$$U_L = (u_{L,\text{domain}} - V_{\text{wall}})(1 - \varepsilon_G), \tag{4}$$

where the gas holdup ε_G is the bubble volume divided by the unit cell volume. Note that $u_{L,\text{domain}}$ is non-zero in our simulations,

$$\varepsilon_G = \frac{\text{bubble volume}}{L_{UC}\pi d_c^2/4}. \tag{5}$$

The superficial gas velocity is calculated from

$$U_G = \varepsilon_G V_b. \tag{6}$$

The volumetric flow of liquid through the thin film surrounding the bubble, Q_{film}, is calculated from the following relation derived by Thulasidas et al. (1995) using a mass balance over a cross section through the bubble and a cross section through the liquid slug:

$$A_b V_b = A_c U_{LS} + Q_{\text{film}}, \tag{7}$$

where U_{LS} is the velocity of the liquid slug that is determined from

$$U_{LS} = u_{L,\text{domain}} - V_{\text{wall}}. \tag{8}$$

Rearranging Eq. (7) we get

$$Q_{\text{film}} = \frac{\pi}{4}(d_b^2 V_b - d_c^2 U_{LS}). \tag{9}$$

The film flow Q_{film} calculated from Eq. (9) agrees with the value obtained by integration of the velocity profile in the film between the bubble surface and the capillary wall.

The converged hydrodynamics obtained were used in a subsequent *third campaign* for wall mass transfer using the fine grid, carried out in a transient manner, for which 3000–10,000 time steps of 0.01 s were used. To correctly capture the steep concentration gradients near the wall, we used a cell size smaller than 1 μm close the wall, with an exponential increase away from the wall, as shown in Fig. 4. The grid details are specified in Table 1. The fineness of the grid was chosen such that the calculated mass transfer coefficient was unaffected by further grid refinement, as discussed in our earlier work (van Baten and Krishna, 2004b). The tracer concentration throughout the system was initially set to zero. At $t = 0$, the tracer concentration at the wall was set to unity (a.u.) to determine the mass transfer from the solid phase to the liquid phase. The following equation is solved for the mass tracer:

$$\frac{\partial}{\partial t}(\rho_L C_L) + \nabla \cdot (\rho_L \mathbf{u}_L C_L - Đ\rho_L \nabla C_L) = 0. \tag{10}$$

Here, C_L is the concentration of mass-tracer in the liquid (a.u.) and $Đ$ is the diffusion coefficient of mass tracer in the liquid. At the top and bottom, the periodic boundary conditions were used: $C_{L,\text{top}} = C_{L,\text{bottom}}$. Though the periodic boundary condition for the tracer is not strictly true, it must be borne in mind that during one "simulation cycle" the amount of mass transferred is negligibly small. Essentially we are assuming a well-mixed liquid phase during one simulation cycle. For each run, the liquid circulates from top to bottom about 1000 times. We have estimated that the error in assuming $C_{L,\text{top}} = C_{L,\text{bottom}}$ is at most 0.03%. Zero tracer flux was allowed through the bubble surface:

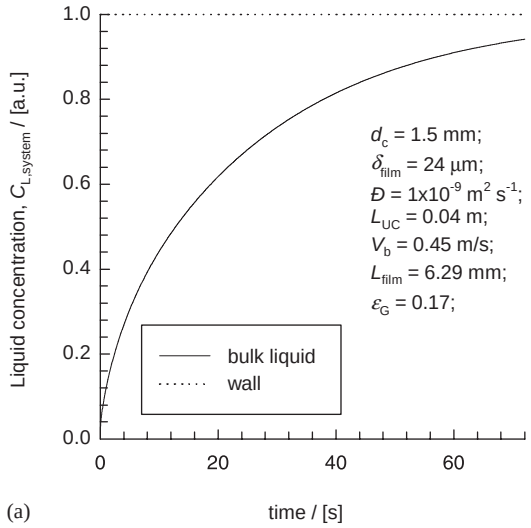

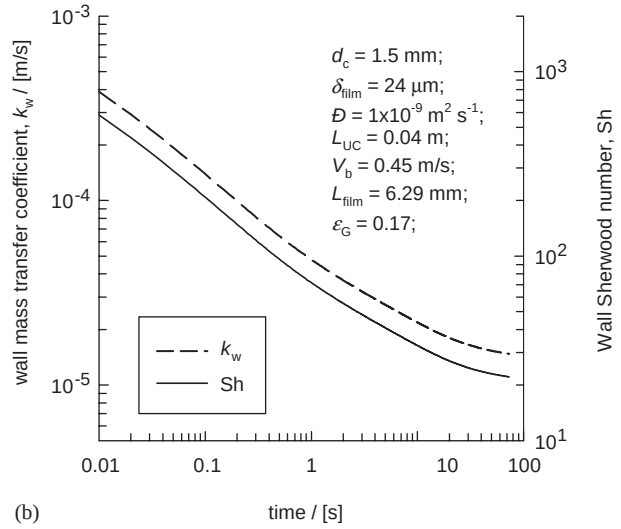

Fig. 5. (a) Concentration versus time profile and (b) time-averaged wall mass transfer coefficient and Sherwood numbers as a function of time. The hydrodynamic parameters are $d_c = 1.5$ mm, $V_b = 0.45$ m/s, $L_{UC} = 0.04$ m, $\delta_{film} = 24$ μm, $\varepsilon_G = 0.17$, $L_{film} = 6.29$ mm. Animations showing the dynamics of mass transfer can be viewed on our website (van Baten and Krishna, 2004a).

$dC_L/dn = 0$. Symmetry conditions apply to the center axis: $dC_L/dr = 0$. At the outer wall, the concentration is specified as $C_{L,w} = 1$.

The total concentration of tracer in the system at each time step is determined from

$$C_{L,\text{system}} = \frac{\sum_{\text{domain}} \text{vol}_i C_{L,i}}{\sum_{\text{domain}} \text{vol}_i}, \tag{11}$$

where the summation is carried out over all the volume elements in the computational domain. A typical concentration–time profile for a 1.5 mm diameter capillary is shown in Fig. 5a.

The wall mass transfer coefficient k_w, averaged over the period $t = 0$ to t is then calculated from

$$\begin{aligned} k_w &= \frac{1}{a_w t} \ln \frac{(C_{L,w} - C_{L,\text{system},t=0})}{(C_{L,w} - C_{L,\text{system}})} \\ &= \frac{1}{a_w t} \ln \frac{(C_{L,w})}{(C_{L,w} - C_{L,\text{system}})} \\ &= \frac{1}{a_w t} \ln \frac{1}{(1 - C_{L,\text{system}})}, \end{aligned} \tag{12}$$

where we introduce the initial condition that the concentration in the system is 0, and that the concentration at the wall is maintained at $C_{L,w} = 1$ during the entire mass-transfer process. In Eq. (12) a_w represents the specific interfacial area for wall mass transfer:

$$a_w = 4/d_c. \tag{13}$$

The Sherwood number can now be calculated from:

$$Sh = \frac{k_w d_c}{Đ}. \tag{14}$$

Both the time-averaged k_w and Sh values decrease with increasing contact time, as demonstrated by a typical example in Fig. 5b.

Since we use periodic boundary conditions, the total length of the capillary tube, L_{tube}, that is traversed in the simulation time, t, is given by

$$t = \frac{L_{\text{tube}}}{V_b}. \tag{15}$$

The wall mass transfer process consists of two separate contributions: (1) wall–slug contribution of the regions in contact with the liquid slug (see Fig. 3b), and (2) wall–film contribution of the region in contact with the liquid film surrounding the bubble (see Fig. 3c). By additionally monitoring the mass transfer fluxes of the wall–slug and wall–film regions at each instant of time, we can also separately determine the Sherwood numbers for these two regions, $Sh_{\text{wall–slug}}$, $Sh_{\text{wall–film}}$, respectively, after averaging from $t = 0$ to t.

A total of 46 simulations with varying parameter values d_c, V_b, L_{UC}, ε_G, δ_{film}, and $Đ$ were carried out on Linux PCs with a single AMD XP processor. The details of parameter values used in these simulations are listed in Table 1. The range of parameter values was chosen to correspond with those obtained in experimental studies (Vandu et al., 2005). Each hydrodynamic simulation on the coarse grid was solved in a matter of minutes, each hydrodynamic simulation on the fine grid took several hours. Each dynamic mass tracer run also took several hours. Animations showing the dynamics of wall mass transfer can be viewed on our website (van Baten and Krishna, 2004a).

3. CFD simulation results

The Sh–Gz_{tube} relationship for all these 46 simulations are shown by the continuous solid ($d_c = 3$ mm), dashed–dot ($d_c = 2$ mm), and dashed ($d_c = 1.5$ mm) lines in Figs. 2a and b. The CFD simulations are in reasonable agreement with the experimental data of Bercic and Pintar (1997) and Horvath et al. (1973). We now proceed to examine in some detail the precise nature of the Sh–Gz_{tube} dependence with the aim of developing a usable correlation of the CFD data.

Consider first the *hydrodynamics* in the 2 mm capillary with a unit cell length $L_{UC} = 0.1$ m, with varying values of the Taylor bubble rise velocity, V_b. The liquid phase velocity profiles at the top of the computational domain (liquid outlet) are shown in Fig. 6a, in the reference velocity frame with a stationary wall (these values are obtained by adding the bubble rise velocity to the values obtained from the simulations. The velocity profiles are parabolic in shape with a maximum velocity at the centre of the channel that is twice the value of the liquid slug velocity, U_{LS}. The liquid velocity profiles within the film are shown in Fig. 6b. The velocity of the liquid at the surface of the film is one and a half times the average liquid velocity, in keeping with the classical solution for the velocity fields in falling films (see Sherwood et al., 1975, p. 78). In Fig. 6c, we see that the magnitude of the velocity of the liquid film at the surface next to the Taylor bubble, V_{film}, increases linearly with V_b. Since the bubble rises upwards *counter-current* to the liquid film the contact time, t_{film}, between the bubble and the liquid film for a film of length L_{film} can be calculated using $t_{\text{film}} = L_{\text{film}}/(V_b + V_{\text{film}})$ where we note that V_{film} has a negative value, as shown in Fig. 6c. The value of $(U_G + U_L)$ is slightly smaller than the value of the bubble rise velocity, V_b and this is due to the backflow of liquid through the film as described by Eq. (7) (see Fig. 6d). With increasing V_b the flow of liquid through the film surrounding the bubble,

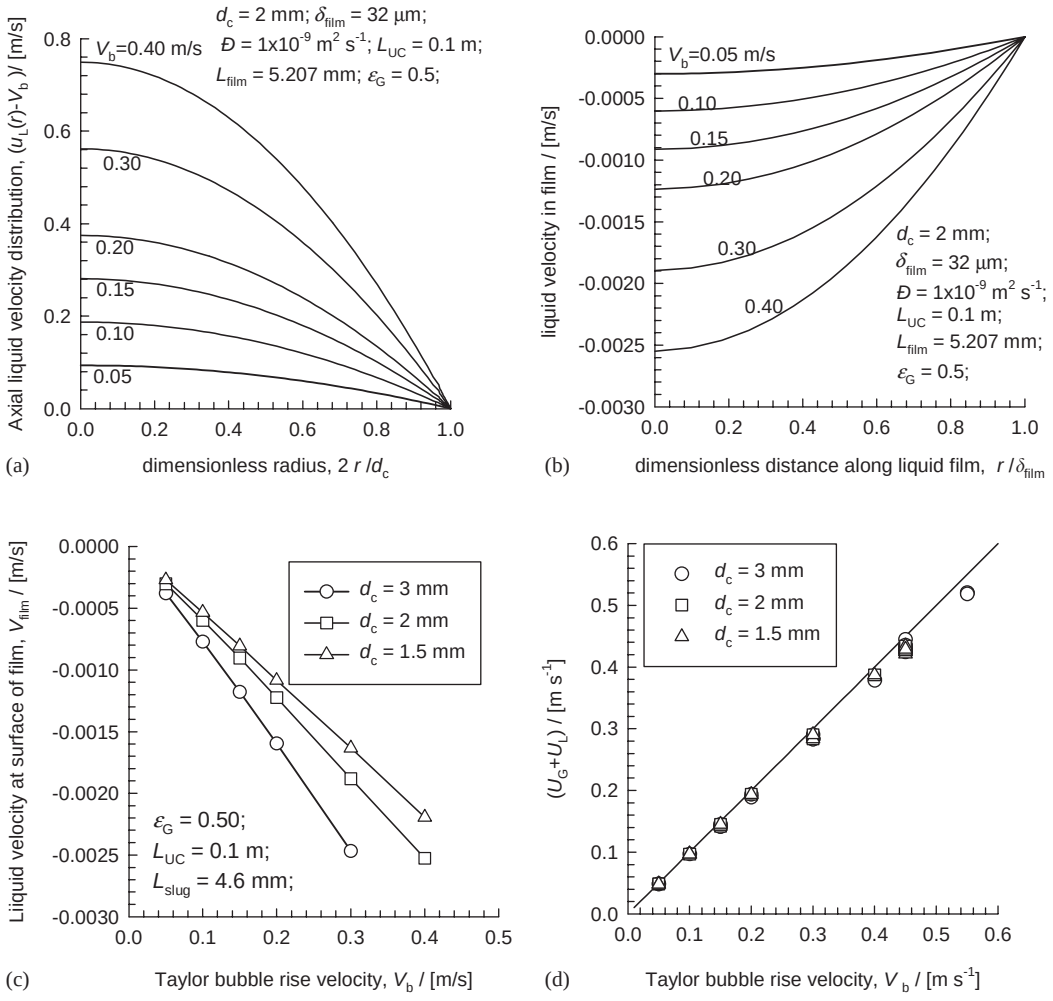

Fig. 6. Radial distribution of liquid velocity (a) at the outlet of the computational domain cell and (b) within the film surrounding the bubble. In these simulation campaigns $d_c = 2$ mm, L_{UC}=0.1 m, $\delta_{\text{film}} = 32$ μm, $\varepsilon_G = 0.5$, $L_{\text{film}} = 5.207$ mm, and $Đ = 1 \times 10^{-9}$ m^2/s. The velocity profiles in (a) and (b) are in the reference frame with respect to a stationary wall. (c) Dependence of surface velocity of the liquid film on the bubble rise velocity V_b for different channel diameters, $d_c = 1.5$, 2 and 3 mm. (d) Dependence of $(U_G + U_L)$ on the bubble rise velocity V_b for channel diameters $d_c = 1.5$, 2 and 3 mm.

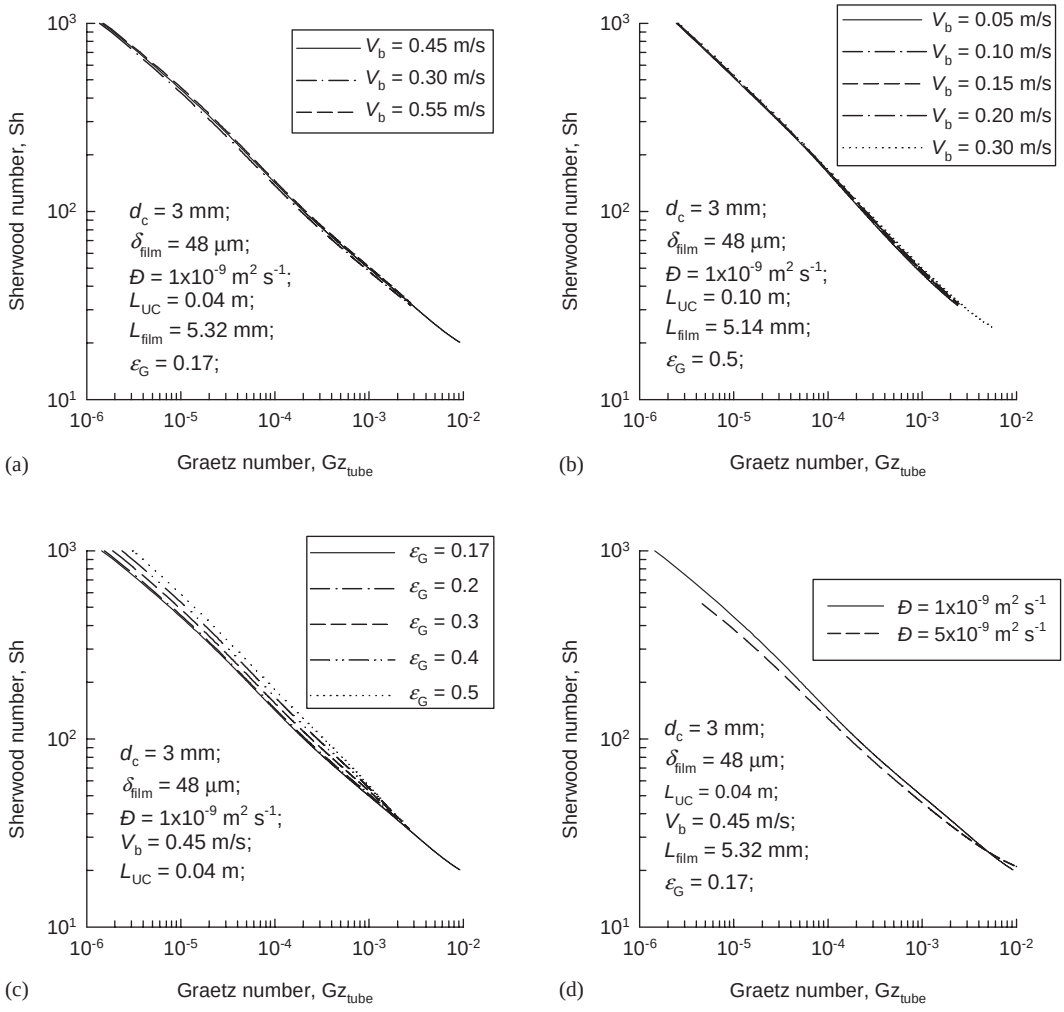

Fig. 7. The wall Sherwood number plotted against Gz_{tube} for 3 mm capillary. (a) Campaign for L_{UC}=0.04 m, $Đ = 1 \times 10^{-9}\,\text{m}^2/\text{s}$, $\varepsilon_G = 0.17$ with varying Taylor bubble rise velocities, V_b. (b) Campaign for L_{UC}=0.1 m, $Đ = 1 \times 10^{-9}\,\text{m}^2/\text{s}$, $\varepsilon_G = 0.5$ with varying Taylor bubble rise velocities, V_b. (c) Campaign for $L_{UC} = 0.04\,\text{m}$, V_b=0.45 m/s, $Đ = 1 \times 10^{-9}\,\text{m}^2/\text{s}$, $\varepsilon_G = 0.17$ with varying gas holdup values ε_G. (d) Campaign for L_{UC}=0.04 m, $V_b = 0.45\,\text{m/s}$, $\varepsilon_G = 0.17$ with varying liquid phase diffusivity values $Đ$.

Q_{film} also increases, thus increasing backflow. This explains the increasing deviation between $(U_G + U_L)$ and V_b with increasing V_b.

We now consider the influence of various parameters on wall *Sh*, expressed as a function of $Gz_{\text{tube}} \equiv L_{\text{tube}}(1-\varepsilon_G)Đ/d_c^2 V_b \equiv t(1-\varepsilon_G)Đ/d_c^2$. Typical simulation results for the 3 mm capillary are shown in Fig. 7 for a variety of conditions. Consider first a campaign in which the unit cell length, gas holdup, and liquid diffusivity are both held constant at $L_{UC} = 0.04\,\text{m}$, $\varepsilon_G = 0.17$ and $Đ = 1 \times 10^{-9}\,\text{m}^2/\text{s}$, respectively. Varying the Taylor bubble rise velocity V_b in the range 0.3–0.55 m/s, yields result that are practically indistinguishable from one another (see Fig. 7a). This would lead us to conclude that the *Sh*–Gz_{tube} relation is not dependent on V_b. This independence on V_b is further confirmed for simulations in which we maintain $L_{UC} = 0.1\,\text{m}$, $\varepsilon_G = 0.5$ and $Đ = 1 \times 10^{-9}\,\text{m}^2/\text{s}$ and vary V_b in the range 0.05–0.30 m/s (see Fig. 7b). In the campaign shown in Fig. 7c the Taylor bubble velocity, unit cell length and liquid diffusivity are held constant at V_b=0.45 m/s, L_{UC}=0.04 m and $Đ = 1 \times 10^{-9}\,\text{m}^2/\text{s}$, respectively, and the gas holdup ε_G is allowed to vary in the range 0.17–0.5. We note that the *Sh*–Gz_{tube} relationship is only marginally influenced by the gas holdup ε_G despite the large variation in the gas holdup. This is because the definition of Gz_{tube} includes the liquid holdup. There is a modest, residual, influence of gas holdup on the *Sh*–Gz_{tube} relationship because the liquid slug length varies when we vary the gas holdup. A shorter liquid slug length yields a higher value of *Sh*; this result is in agreement with the Horvath data presented in Fig. 2b. In the campaign shown in Fig. 7d the liquid diffusivity $Đ$ is varied by a factor 5 from 1×10^{-9} to $5 \times 10^{-9}\,\text{m}^2/\text{s}$, keeping $V_b = 0.45\,\text{m/s}$, L_{UC} = 0.04 m and ε_G = 0.17. We note that the *Sh*–Gz_{tube} relationship is dependent on the liquid-phase diffusivity $Đ$. A higher liquid diffusivity leads to a lower *Sh*. The reason for this observation is not intuitively obvious and an explanation is given below. Exactly analogous results as shown in Fig. 7 were obtained with the 1.5 and 2.5 mm diameter capillaries.

To gain further insights into the reasons why Sh–Gz_{tube} relationship is influenced by the gas holdup, slug length and liquid diffusivity, we examine the contributions of the wall–slug and wall–film regions separately. In Fig. 8a we show the simulation results, obtained in the 1.5 mm diameter capillary, for Sherwood numbers for the total wall region (as presented in the foregoing discussions), along with the corresponding values for the wall–slug and wall–film regions for a unit cell length $L_{UC} = 0.1\,\text{m}$, with $\varepsilon_G = 0.5$ and $V_b = 0.05\,\text{m/s}$. The wall–film mass transfer is significantly poorer than that of the wall–slug region. Since the wall–film area is 50% of the total wall area, the poorer film mass transfer contribution causes the Sh for total wall to be significantly lower than that for the wall–slug region alone. A further reason for poorer Sh for wall–film is that for long films, i.e., long contact time between bubble and film (i.e., low V_b), the film is most likely nearing saturation conditions. This point has also been discussed by Kreutzer (2003) in some detail. For shorter films and shorter contact times between film and bubble all three Sh numbers are close to one another, as is evidenced by the simulation results shown in Fig. 8b for L_{UC}=0.04 m, V_b=0.05 m/s and ε_G=0.17. The detrimental effect of saturation in the liquid film surrounding the Taylor bubble is even more pronounced for long films *and* high liquid diffusivities. This is illustrated in Fig. 8c for $L_{UC} = 0.1\,\text{m}$, $\varepsilon_G = 0.5$, $V_b = 0.10\,\text{m/s}$ and $Đ = 5 \times 10^{-9}\,\text{m}^2/\text{s}$. The film Sh is about one order of magnitude lower than the wall–slug value because the saturation of the film is much easier for higher diffusivity values.

For a given set of hydrodynamic parameters, the Sh–Gz_{tube} relationship is additionally dependent on the capillary diameter d_c as illustrated in the simulation results shown in Figs. 9a and b for two sets of conditions as specified in the legend. The reason for the dependence on the capillary diameter is because the film thickness δ_{film} is smaller for the smaller diameter capillary. This smaller film thickness causes the film contribution to be poorer because of the approach to saturation within the film.

On the basis of a systematic analysis of all the 46 simulations, we derived the following correlation for the Sherwood number, for the *total* wall region:

$$Sh = \frac{\beta}{Gz_{\text{tube}}^{\alpha}}, \quad \alpha = 0.61 Gz_{\text{slug}}^{0.025}, \quad \beta = \frac{0.5}{(Gz_{\text{slug}}/\varepsilon_G)^{0.15}},$$
$$Gz_{\text{slug}} = \frac{L_{\text{slug}} Đ}{d_c^2 V_b}. \tag{16}$$

This correlation reflects that fact the α and β in the $Sh = \beta/Gz_{\text{tube}}^{\alpha}$ function is dependent on ε_G, L_{slug} and $Đ$ as emphasized in the discussions surrounding Fig. 7. Eq. (16) is valid for Gz_{tube} values lower than 0.01. For values of Gz_{tube} higher than 1 the Sh number tends to reach asymptotic values. However, values $Gz_{\text{tube}} > 0.01$ are not often realized in practice because this would inordinately long tubes. A further point to note is that the dependence of α on Gz_{slug} is only very weak and its calculation requires knowledge of the slug length. For a wide range of parameter values, the variation in the value of α is in the range of 0.45–0.52 and so a constant value of 0.48 may also be used for rough estimations.

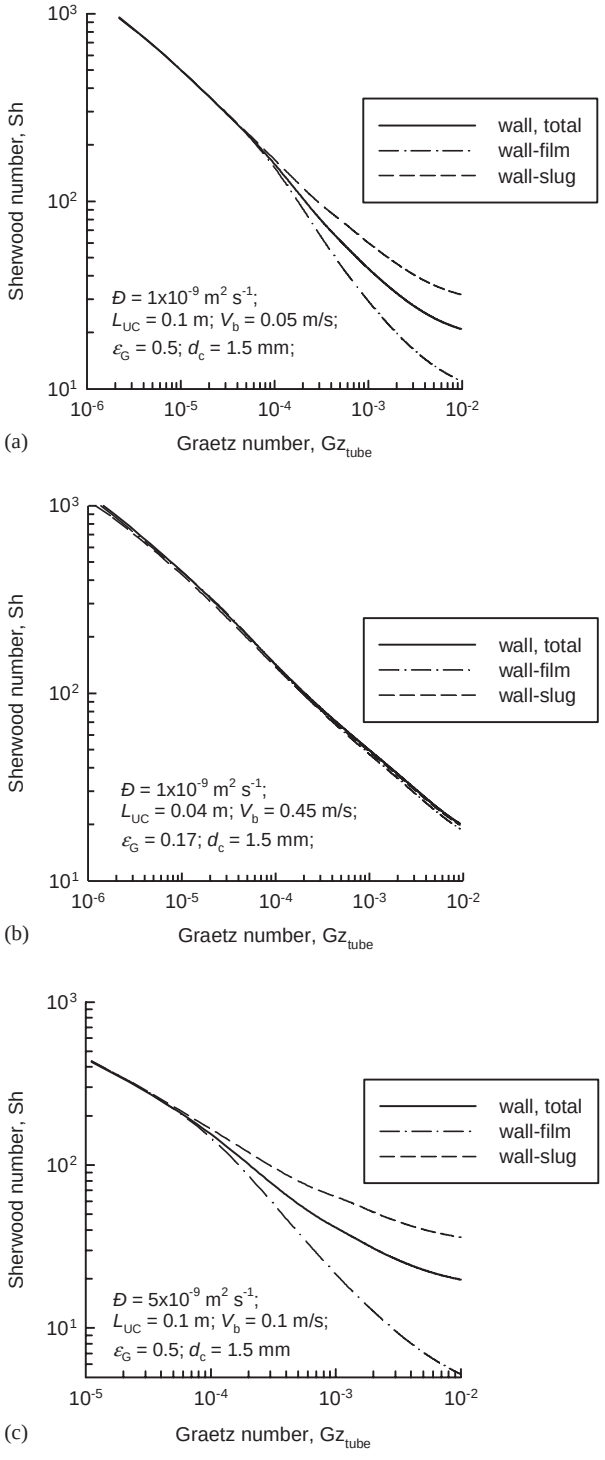

Fig. 8. Comparison of the wall (total), wall–film and wall–slug Sherwood numbers as a function of Gz_{tube} for 1.5 mm capillary. (a) Campaign for L_{UC}=0.1 m, $Đ = 1\times10^{-9}\,\text{m}^2/\text{s}$, $\varepsilon_G = 0.5$, $V_b = 0.05\,\text{m/s}$. (b) Campaign for L_{UC}=0.04 m, $Đ = 1 \times 10^{-9}\,\text{m}^2/\text{s}$, $\varepsilon_G = 0.17$, $V_b = 0.45\,\text{m/s}$. (c) Campaign for L_{UC}=0.1 m, $Đ = 5\times10^{-9}\,\text{m}^2/\text{s}$, $\varepsilon_G = 0.5$, $V_b = 0.1\,\text{m/s}$.

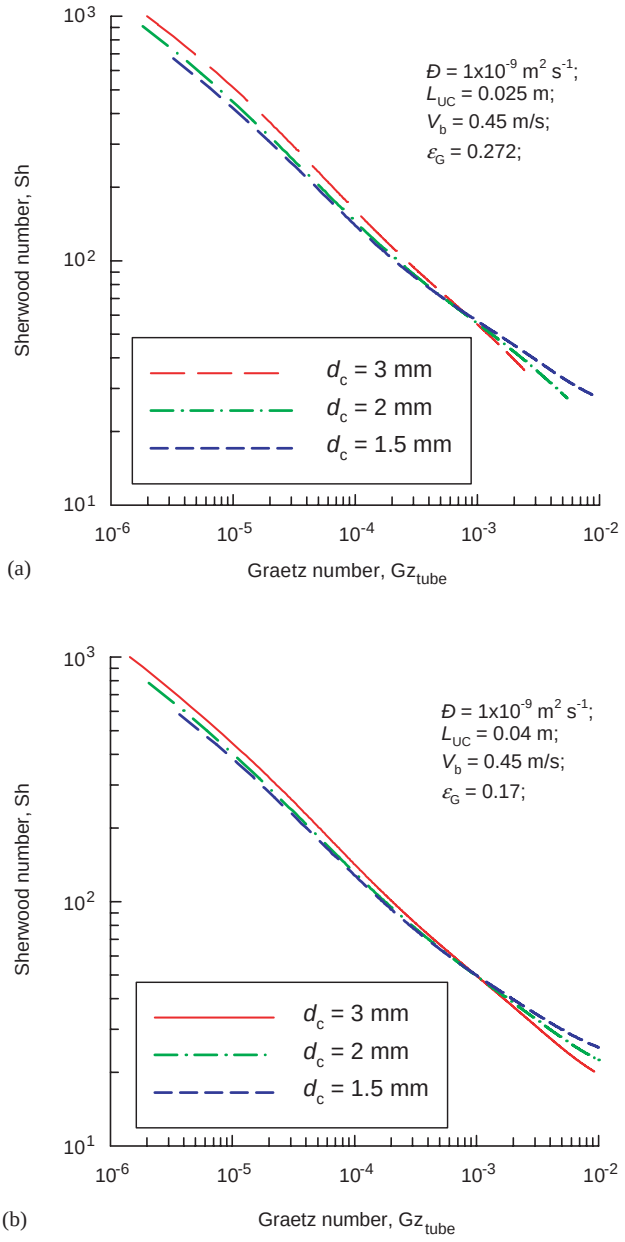

Fig. 9. Comparison of Sherwood number versus Gz_{tube} relationships for 1.5, 2 and 3 mm capillaries. (a) Campaign for L_{UC}=0.025 m, $Đ = 1 \times 10^{-9}$ m^2/s, $\varepsilon_G = 0.272$, V_b=0.45 m/s. (b) Campaign for L_{UC}=0.04 m, $Đ = 1 \times 10^{-9}$ m^2/s, $\varepsilon_G = 0.17$, $V_b = 0.45$ m/s.

Fig. 10 compares the experimentally determined values of *Sh* by Bercic and Pintar (1997) and Horvath et al. (1973) against the predictions using Eq. (16). We note that the agreement is reasonably good, when we consider the scatter in the experimental data.

The corresponding correlation for the wall–slug region alone is somewhat simpler:

$$Sh_{\text{wall–slug}} = \frac{2.4 + 1.5/(L_{\text{slug}}/d_c)}{Gz_{\text{tube}}^{0.45}}. \quad (17)$$

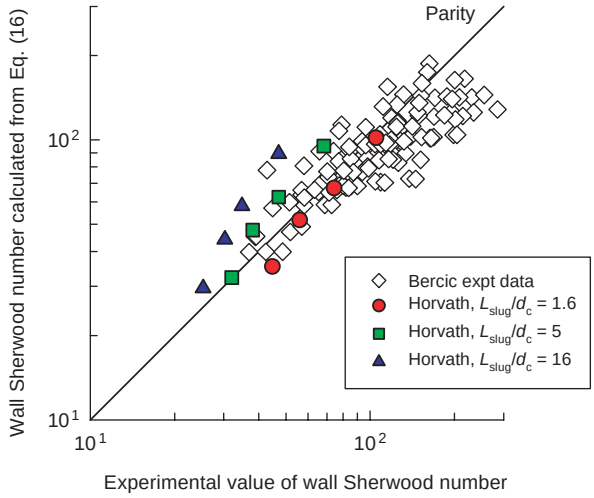

Fig. 10. Parity plot of experimentally determined values of Sherwood number by Bercic and Pintar (1997) and Horvath et al. (1973) against the predictions using Eq. (16). In addition to the parameters specified in the paper by Bercic and Pintar (1997), it should be noted that the 2.5 mm capillary had a length $L_{\text{tube}} = 0.35$ m, the 3.2 mm capillary had lengths of 0.25–0.27 m.

4. Conclusions

We have used CFD simulations to investigate mass transfer from the liquid phase to the wall during rise of Taylor bubbles in circular capillaries. The Sherwood number for wall mass transfer decreases significantly with increasing values of Gz_{tube}. The precise dependence of *Sh* on Gz_{tube} depends on a variety of hydrodynamic parameters such as slug length, gas holdup, liquid diffusivity. By fitting the CFD simulations we have derived the empirical correlation (16) for practical estimation of wall mass transfer from information on Taylor flow hydrodynamics.

Notation

a	gas–liquid interfacial area per unit cell volume, m^2/m^3
A	cross sectional area, m^2
C	concentration of tracer in liquid phase, a.u.
d_c	capillary diameter, m
d_b	bubble diameter; see Fig. 1(a), m
$Đ$	liquid phase diffusivity, m^2/s
$\mathbf{g}$	gravitational vector, m/s^2
Gz_{tube}	Graetz number based on tube length ($\equiv L_{\text{tube}}(1-\varepsilon_G)Đ/d_c^2 V_b$), dimensionless
Gz_{slug}	Graetz number based on slug length ($\equiv L_{\text{slug}}Đ/d_c^2 V_b$), dimensionless
k_w	wall-mass transfer coefficient, m/s
L_{film}	length of liquid film (see Fig. 1a), m
L_{slug}	length of liquid slug, $L_{\text{slug}} = L_{UC}(1-\varepsilon_G)$, m
L_{tube}	total length of capillary tube (see Fig. 1a), m
L_{UC}	unit cell length, m
n	vector normal to the surface, dimensionless

p	system pressure, Pa
Q_{film}	volumetric liquid film flow; m^3/s
r	radial coordinate, m
Sh	Sherwood number for wall mass transfer ($\equiv k_w d_c/Đ$),dimensionless
t	time, s
t_{film}	contact time of liquid film with Taylor gas bubble, m/s
$\mathbf{u}$	liquid velocity vector, m/s
u	velocity in z-direction, m/s
U_G	superficial gas velocity, m/s
U_L	superficial liquid velocity, m/s
U_{LS}	mean velocity of liquid slug, m/s
vol_i	volume of cell i, m^3
V_b	Taylor bubble rise velocity, m/s
V_{film}	velocity at surface of liquid film, next to bubble, m/s
V_{wall}	velocity of wall boundary condition in simulations, equal to $-V_b$, m/s
z	axial coordinate, m

Greek letters

δ_{film}	thickness of film surrounding bubble, m
ε_G	gas holdup, dimensionless
μ_L	liquid viscosity, Pa s
ρ_L	density of liquid phase, kg/m^3

Subscripts

b	refers to Taylor bubble
bottom	bottom boundary of computational domain
c	refers to capillary
domain	in computational space
film	refers to liquid film
G	refers to gas phase
L	refers to liquid phase
i	referring to cell number i
r	in radial direction
s	at the bubble surface
slug	referring to liquid slug
system	referring to the computational system
top	top boundary of computational domain
tube	referring to capillary tube
UC	refers to unit cell
wall	refers to wall
z	in axial direction
$\perp$	perpendicular

Acknowledgements

We are grateful to Dr. G. Bercic for providing us the experimental data reported in his 1997 paper in electronic format for reanalysis and replotting purposes. The critical comments of Dr. Bercic on the draft manuscript are most appreciated. The Netherlands Organisation for Scientific Research (NWO) is gratefully acknowledged for providing financial assistance in the form of two grants: *Programmasubsidie* and *TOP subsidie* for development of novel concepts in reactive separations technology and for reactor intensification.

References

Bercic, G., Pintar, A., 1997. The role of gas bubbles and liquid slug lengths on mass transport in the Taylor flow through capillaries. Chemical Engineering Science 52, 3709–3719.

Boger, T., Roy, S., Heibel, A.K., Borchers, O., 2003. A monolith loop reactor as an attractive alternative to slurry reactors. Catalysis Today 79, 441–451.

Edvinsson, R.K., Cybulski, A., 1995. A comparison between the monolithic reactor and the trickle-bed reactor for liquid-phase hydrogenations. Catalysis Today 24, 173–179.

Horvath, C., Solomon, B.A., Engasser, J.M., 1973. Measurement of slug flow using radial transport in enzyme tubes. Industrial and Engineering Chemistry Fundamentals 12, 431–439.

Irandoust, S., Andersson, B., 1988. Mass-transfer and liquid-phase reactions in a segmented two-phase flow monolithic catalyst reactor. Chemical Engineering Science 43, 1983–1988.

Kreutzer, M.T., 2003. Hydrodynamics of Taylor flow in capillaries and monolith reactors. Ph.D. Thesis, Delft University of Technology, Delft, The Netherlands.

Kreutzer, M.T., Du, P., Heiszwolf, J.J., Kapteijn, F., Moulijn, J.A., 2001. Mass transfer characteristics of three-phase monolith reactors. Chemical Engineering Science 56, 6015–6023.

Nijhuis, T.A., Kreutzer, M.T., Romijn, A.C.J., Kapteijn, F., Moulijn, J.A., 2001. Monolithic catalysts as more efficient three-phase reactors. Catalysis Today 66, 157–165.

Rhie, C.M., Chow, W.L., 1983. Numerical study of the turbulent flow past an airfoil with trailing edge separation. AIAA Journal 21, 1525–1532.

Roy, S., Heibel, A.K., Liu, W., Boger, T., 2004. Design of monolithic catalysts for multiphase reactions. Chemical Engineering Science 59, 957–966.

Shah, R.K., London, A.L., 1978. Laminar flow forced convection in ducts: a source book for compact heat exchanger analytical data. In: Shah, R.K., London, A.L. (Eds.), Advances in Heat transfer: Supplement 1. Academic Press, New York.

Sherwood, T.K., Pigford, R.L., Wilke, C.R., 1975. Mass Transfer, McGraw-Hill, New York, USA.

Stankiewicz, A., 2001. Process intensification in in-line monolithic reactor. Chemical Engineering Science 56, 359–364.

Thulasidas, T.C., Abraham, M.A., Cerro, R.L., 1995. Bubble-train flow in capillaries of circular and square cross-section. Chemical Engineering Science 50, 183–199.

van Baten, J.M., Krishna, R., 2004a. Mass Transfer for Taylor flow in Capillaries. University of Amsterdam, Amsterdam, The Netherlands, http://ct-cr4.chem.uva.nl/taylor_cfd, 12 March.

van Baten, J.M., Krishna, R., 2004b. CFD simulations of mass transfer from Taylor bubbles rising in circular capillaries. Chemical Engineering Science 59, 2535–2545.

van Doormal, J., Raithby, G.D., 1984. Enhancement of the SIMPLE method for predicting incompressible flows. Numerical Heat Transfer 7, 147–163.

Vandu, C.O., Ellenberger, J., Krishna, R., 2005. Hydrodynamics and mass transfer in an upflow monolith loop reactor. Chemical Engineering and Processing 44, 363–374.